AIAA-2026-0287

Fluidic Control of the Flow within a Diffuser with Variable Bend

Joshua W. Fletcher[1], Samuel Li[2], Bojan Vukasinovic[3], James Mace[4], and Ari Glezer[5]
Woodruff School of Mechanical Engineering, Georgia Institute of Technology, Atlanta, GA, USA
Mory Mani[6]
Massachusetts Institute of Technology, Cambridge, MA, USA
Zachary T. Stratton[7] and John T. Spyropoulos[8]
Naval Air Warfare Center – Aircraft Division, Patuxent River, MD, USA

A flow control approach to address total pressure distortions at the AIP of a modular diffuser testbed with a variable bend section ($20° \le \theta \le 60°$, $0.2 \le r/D \le 0.5$) was developed and tested in a joint experimental/numerical study. In this approach, fluidic actuation that is applied downstream of the interchangeable bend configurations is devised to counter the transport of streamwise vorticity concentrations of opposite sense along the bend's inner radius surface that subsequently roll into counter rotating vortices, are advected through the diffuser to the AIP, and induce total pressure deficit and distortion. Experimental and numerical investigations of the control approach that utilized spanwise arrays of yawed wall jets demonstrated successful suppression and delay of vorticity transport within the diffuser within $0.3 \le M \le 0.5$. It is shown that a single wall jet array downstream of the bend can effectively reduce distortion and improve recovery across bend geometries at bend angles and radii up to 60° and down to $0.2D$, respectively, reducing the baseline distortion level by 55% at thrust-based momentum coefficient $C_\mu^F = 0.02$. Moreover, optimization of the number of active jets can further reduce the baseline distortion by 60% at $C_\mu^F = 0.014$ when only 60% of the original jet array is active.

Nomenclature

AFC = Active flow control
AIP = Aerodynamic interface plane

---

[1] Graduate Research Assistant, AIAA Member
[2] Graduate Research Assistant, AIAA Member
[3] Senior Research Engineer, AIAA Member
[4] Consultant, AIAA Member
[5] Professor, AIAA Fellow
[6] Consultant, AIAA Member
[7] Aerospace Engineer, NAWCAD, AIAA Member
[8] Aerospace Engineer - Lead for Inlets, Nozzles, and Aeroacoustics, NAWCAD, AIAA Associate Fellow

AR = Inlet/channel aspect ratio
C_q = Jet mass flow rate coefficient
C_μ = Jet momentum coefficient
D_{AIP} = AIP diameter
$DPCP_{avg}$ = Average circumferential distortion parameter
L = throat-to-AIP length
r = Radius of curvature at the bend
r/D = Radius of curvature at the bend normalized by AIP diameter
M = Mach number
M_{AIP} = Mach number at the aerodynamic interface plane
θ = Bend turning angle
ω = Vorticity

I. Introduction

The development of next-generation military aircraft features streamlined propulsion/airframe integration and highlights the need for increasingly compact and complex engine inlet designs. These lower form factor inlets and diffusers allow for greater freedom of airframe design and potential drag and performance improvements. However, such compact and complex inlet apertures often include highly offset or serpentine-shaped diffusers and therefore pose significant challenges for managing their adverse internal flow characteristics. High-speed subsonic flows within offset diffusers are dominated by intense streamwise vortices, possible flow separation at moderate to high turning angles, and/or even a potential appearance of transonic shock. Without appropriate flow-management techniques, these secondary flow effects can cause significant total pressure losses, as well as distortion at the aerodynamic interface plane (AIP), leading to undesired aeromechanical interactions with the downstream compression fan blades, compromising turbomachinery operability and performance.

Inlet concepts for future aircraft feature highly compact characteristic lengths in addition to aggressive centerline offsets with significant curvature exceeding existing design heritage. Connolly et al. [1] simulated the flow through a serpentine diffuser and found that the secondary flows were driven by a pair of counter-rotating Dean vortices [2]. Though Dean vortices have primarily been investigated in the context of low-speed flow through bends, the same flow physics characterizes flow within curved diffusers at higher duct-flow speeds. Dean [2, 3] analyzed flow through a curved pipe at low Reynolds numbers and found the flow is characterized by a pair of counterrotating streamwise vortices, known as Dean vortices, formed due the competing effects of the centrifugal force and pressure gradient. Towards the center of the bend, the fluid streamline is driven from the inner radius towards the outer radius due to the centrifugal force. However, viscosity near the surface of the upper and lower walls diminishes the effect of the centrifugal force, and the inward-directed pressure gradient instead dominates. The Dean number is defined as: $De = Re\sqrt{D_h/R_c}$, where Re is the Reynolds number, D_h is the hydraulic diameter of the pipe, and R_c is the radius of curvature of the bend. This value quantifies this secondary flow phenomenon, its shape, and its general structure. More recently, numerical and experimental investigations have further validated these findings and expanded on the mechanisms underlying their formation. Dutta et al. [4] used a k-ε model and showed that though the vortices are initially formed near the outer perimeter of the duct, the curvature also induces a recirculation region that advects the vortices such that they coalesce at the inner bend of the duct. They also found that the bend angle plays a significant role in the formation and structure of the streamwise vortices that are unaccounted for in the Dean number. Additionally, Winters [5] performed a numerical analysis of laminar flow through a rectangular bend and found that in the presence of strong pressure gradients, Dean vortices can split into a four-cell flow pattern, and by changing the aspect ratio of the bend, the formation of these four-cell flow patterns can further evolve. Sudo et al. [6] used hot wire anemometry to experimentally analyze turbulent flow through a 90° rectangular/square bend. They found that although the intensity of the secondary flows was maximum at the bend exit, they remained significant downstream of the bend. Additionally, past the bend, the turbulent kinetic energy continued to grow, where it reached its maximum downstream of the bend exit. However, nearly all studies conducted on curved ducts have focused on a low Reynolds number, incompressible flows. There is a demonstrated need to extend these investigations into the compressible flow regime relevant to advanced inlet systems.

Over recent decades, passive and active flow control techniques have been developed and investigated to reduce the adverse effects of integrated inlet flow on propulsion system performance. Passive vortex generators have been used to improve recovery and reduce distortion by affecting the evolution of secondary flow vortices [7] and partially suppressing internal separation [8-10]. While these passive techniques have had varying successes, they present disadvantages compared to active flow control (AFC) as their presence lead to total pressure losses, and their passive nature means they lack the flexibility to adapt to changing flow conditions. To this end, many AFC approaches have been designed and tested. Scribben et al. [11] used microjets in a serpentine diffuser to reduce distortion by 70% and improve total pressure recovery by 2% at an AIP Mach number of 0.55 and jet mass flow rate coefficient C_q =0.01. Anderson et al. [12] numerically investigated a redesigned M2129 inlet s-duct and used optimized microjets to reduce DC60 (lowest pressure in 60° sector) distortion parameter below 0.1 with $C_q = 0.005$. Gartner and Amitay [13] used pulsed jets, sweeping jets, and a blowing slot to improve total pressure recovery in a rectangular diffuser, and showed that the slot-jet was less effective than pulsed or sweeping jets. Rabe [14] evaluated microjets in a double-offset diffuser driven by a gas-turbine engine and, with the jets driven by the bleed from the engine at a rate of 1%, was able to decrease circumferential distortion by 60% at $M = 0.55$. Harrison et al. [15] experimentally and numerically investigated a suction and blowing scheme for a thick boundary layer ingesting a serpentine diffuser. At $M = 0.85$, they were able to reduce DC60 by 50% with a circumferential blowing scheme, but reduced DC60 by 75% by including suction. Garnier [16] performed spectral analysis comparing pulsed and continuous blowing in an aggressive s-duct using an array of dynamic pressure sensors and concluded that the pulsed blowing could match the performance of continuous jets at half the C_q over $M = 0.2 – 0.4$. Amitay et al. [17] used an array of synthetic jets to completely reattach flow in a serpentine duct up to $M = 0.2$, while Mathis et al. [18] also used synthetic jets to reattach flow through an S-duct diffuser at $Re = 4.1x10^4$. Gissen et al. [19] used a hybrid approach of passive vanes and synthetic jets in a boundary layer ingesting offset diffuser to improve circumferential distortion by 35% at $M = 0.55$. Burrows et al. [20] utilized fluidic-oscillating jets to control the vorticity of a modified offset diffuser and reduced distortion by 68% with $C_q = 0.0025$ at $M = 0.55$. In an extension study, Burrows et al. [21] were able to mitigate the effect of local flow separation in a serpentine diffuser and decreased circumferential distortion by 60% with C_q =0.005. Finally, Burrows et al. [22] added a cowl to the same serpentine geometry that produced strong inlet streamwise vortices and significant total pressure losses. These were mitigated using aerodynamic bleed through the cowl.

These prior efforts clearly showed that AFC technology can be successfully used to mitigate effects of adverse flow features within complex inlet designs. However, in earlier investigations, AFC has been incorporated into pre-existing fixed inlet designs as an *a posteriori* approach for improving performance. This inherently precludes investigating the interaction between flow control actuation and the geometric and operational space during the design stage. The overarching objective of the present project is to demonstrate the effectiveness of incorporating AFC early in the design process, enabling the use of shorter, more compact inlet diffusers. This was preceded by the development of a geometrically adaptive diffuser testbed that allows for rapid exploration of a range of compact-inlet geometric-design configurations as well as numerical simulation tools to allow for rapid variation of desired design characteristics [23]. The experimental testbed was designed and manufactured to allow rapid changes in the bend aspect ratio, angle, and its radius of curvature, as well as changes to the diffuser shape, section lengths, and other parameters. In addition, the setup enables easy integration of AFC at multiple points throughout the diffuser to mitigate the adverse flow effects within the flow path.

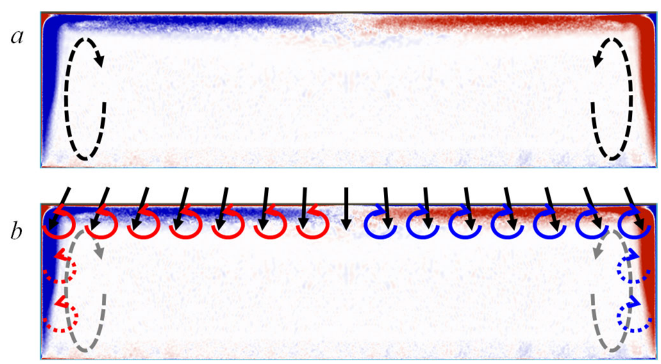

Figure 1. *Renditions of azimuthal transport of streamwise vorticity in the base flow by Dean circulations downstream of the bend (a) and of the present control approach using a spanwise array of yawed surface jets to oppose the transport and accumulation of vorticity in the base flow and inject streamwise vorticity of the opposite sense (b).*

The present effort builds on the earlier work of Stratton et al. [23] and Li et al. [24], who pointed out that the main sources of the flow distortion and losses in the present flow paths are associated with the onset of Dean circulations in the diffusers bend. As discussed in detail by Li et al. [24], flow turning in the bend initiates streamwise vorticity concentrations along the side walls, and it was argued that Dean circulations advect these concentrations along the inner bend as illustrated in Figure 1a. Based on these findings, a flow control approach was devised to counter this vorticity transport over the upper surface using two mirrored spanwise arrays of yawed fluidically-oscillating jets, as shown in Figure 1b to induce small-scale vorticity concentrations of the opposite sense to that of the base flow on either spanwise segment along the upper surface (Figure 1b). While generally effective, this approach had some limitations at higher Mach numbers [24] that were attributed to the placement of the array upstream of the bend. In the present investigation, this shortcoming is addressed by placing similar arrays of steady jets just downstream of the bend exit plane with significant tempering of the evolution of the base flow streamwise vortex pair. The test facility and diffuser design are presented in §II, the numerical setup and methodology are described in §III, and the underlying structure of the base flow is summarized in §IV. Finally, the proposed flow control approach is assessed in §V, its time-resolved characteristics are further discussed in §VI, and an optimized subset of flow control results are described in §VII.

II. Experimental Setup and Flow Diagnostics

The present experiments are performed in the Georgia Tech open-return, pull-down, subsonic wind tunnel driven by a 150 hp blower, as shown schematically in Figure 2, along with the diffuser model that replaces the test section. The programmable diffuser testbed is similar to the diffuser that was used by Li et al. [24], where it is described in more detail. Ambient air is drawn through a bellmouth having an inlet diameter $3.9D_{AIP}$, followed by a circular to rectangular transition to a constant cross-section channel upstream of an interchangeable bend section that is connected to a short diffuser and to the AIP section in which the time-averaged total pressure distribution is measured using a rake of 40 total pressure probes within a round conduit having a diameter D_{AIP} = 12.7 cm. Downstream of the total pressure rake section, the flow is expanded through the tunnel's diffuser and a 90-degree turn into the system's blower that is controlled by a variable frequency drive. The blower's outlet is connected to a flow silencer to reduce noise, and a water-cooled low-pressure drop heat exchanger (not shown) cooled by a chiller controls the return air to within 1-2° C. The design of the bend section incorporates interchangeable mating elements to yield independent variations in aspect ratio, bend turning angle, and turning radius. The present investigations considered 9 bend configurations having rectangular cross section with width-to-height ratio of 4:1, bend radii, r/D= 0.2, 0.35, 0.5, and bend angles θ= 20°, 40°, and 60° that were tested over a range of AIP Mach numbers $0.3 < M_{AIP} < 0.5$. It should be noted that while the model bends are configured horizontally, as shown in Figure 2, the experimental and numerical data are presented for vertical bending with the inner-bend surface at the top.

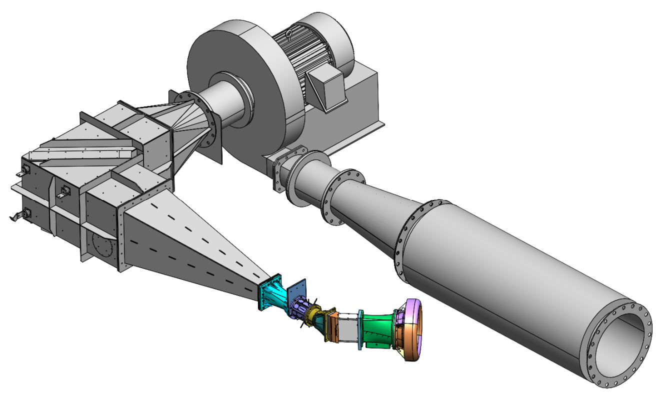

Figure 2. *CAD model of pull-down wind tunnel facility inserting the modular diffuser model as the test section.*

A 40-probe total-pressure rake at the AIP is assembled using eight radial arrays of five total pressure tubes positioned at r/R = 0.27, 0.38, 0.51, 0.67, and 0.9, that are spaced 45° apart azimuthally around the circumference of the AIP. The time-averaged total pressure measurements are used to compute the total pressure recovery as well as the flow distortion descriptors per SAE ARP1420C [25]. The total pressure rakes are supplemented with a matching array of eight static pressure ports that are each located on the diffuser wall, $0.4D$ upstream of the AIP. Another azimuthal array of eight equally spaced static pressure ports is located at the upstream end of the bellmouth and is used to compute the Mach number and mass flow rate through the diffuser using an earlier-developed calibration procedure [23]. The mass flow rate is normalized with respect to standard sea level pressure and temperature. Static and total pressures are measured using a PSI Netscanner system, where each set of pressure measurements is averaged over 64 independent samples, while the time-averaged static and total pressures are computed from fifty such sets. The manufacturer-specified accuracy is ±17.25 Pa, and the overall uncertainty of the time-averaged pressure is less than 1%. The static pressure around the circumference of the bellmouth is measured using a 10 torr MKS Baratron transducer (uncertainty of about 1.5 Pa) that is sampled using a computer-controlled rotary valve.

III. Numerical Setup

Flow Solver and Turbulence Model Large-eddy simulations (LES) are used to simulate the flow through the model presented in this study. The solver employed is charLES [26], which solves the governing equations for the filtered, compressible Navier-Stokes equations for mass, momentum, and total energy. It uses a density-based finite-volume method in which fluxes are computed with a low-dissipation, entropy-preserving spatial discretization that is formally 2nd-order accurate [26]. The time integration is performed using an explicit third-order Runge-Kutta scheme. The solutions are computed on unstructured grids based on Voronoi diagrams generated from a hexagonally close-packed lattice of seed points [27]. The grids generated with this technique results in a smooth mesh of isotropic polyhedral cells, which are well suited for LES.

In the near-wall region, the thin boundary-layer equations are assumed to be valid, yielding a simplified momentum equation for a constant-stress layer in the wall-normal direction. This equation can be solved algebraically and is referred to as the equilibrium stress model [28]. These equations are solved at each wall-adjacent cell centroid at each time step for wall shear stress, which serves as the Neumann boundary conditions for the momentum equations. This wall model does not account for the unsteadiness of the inner-layer solution or the pressure gradient effects. This approach, referred to as wall-modeled LES (WMLES), significantly reduces near-wall grid requirements. To account for sub-grid-scale stresses, the dynamic Smagorinsky model is used [29].

Computational Domain and Simulation Details The computational domain used for the diffuser in this study is shown in Figure 3 and is based on the CAD model of the experimental facility and test model hardware. The AFC module is installed downstream of the bend, shown in purple. In the baseline case, this module is removed and replaced with a simple flat wall. The bellmouth is extended (shown in yellow) to incorporate a sizeable hemispherical inlet region to ensure very low flow velocities in the far field. A total pressure boundary condition is applied to the hemispherical inflow surface, set at standard atmospheric day conditions. A mass flow boundary condition is applied to the AFC plenum inflow surface, such that a known C_q is specified. The AFC array includes jets along both the side walls and the top surface, each of these sets have their own inflow, so that they can be turned on and off independently. The tunnel walls are set as no-slip walls where the algebraic equilibrium wall model is applied. The extensions, downstream of the AIP, are set as free-slip walls. The outlet is a static pressure boundary condition, where the pressure is set to achieve a desired mass flow rate at the AIP. In this study, simulations were conducted at $M_{AIP} = 0.4$ at $\theta = 60^o$ and $r/D = 0.2$ without AFC (i.e. baseline) and with AFC on at $C_q = 0.015$. Three AFC configurations were studied, top jets on only, side jets on only, and both top and side jets active.

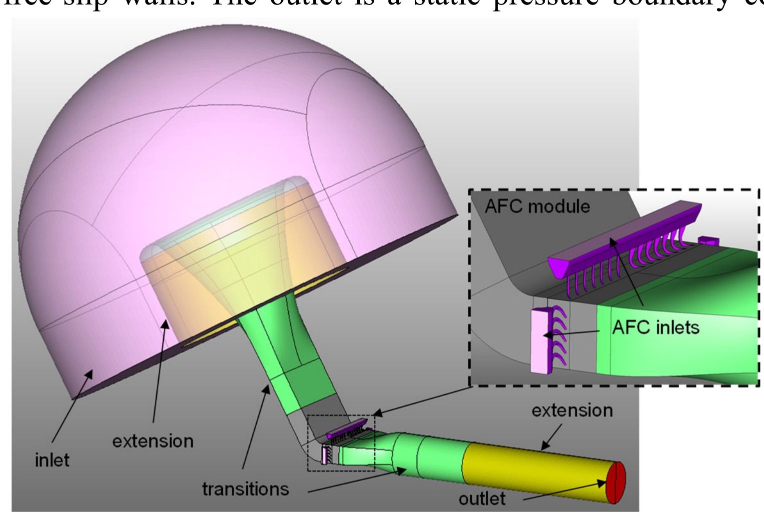

Figure 3. *Computational domain.*

The grids used in this study are based on the findings from the AFC testbed configuration and the grid sensitivity study for the baseline tunnel. Details of the meshes and validation can be found in Stratton et al. [23]. The total number of elements in the computational domain is 250M and 380M for the baseline and AFC configurations, respectively. The average y^+, measured at the gray walls in Figure 3, is 24 and 28 for the baseline and AFC configurations, respectively. All simulations were run on the U.S. Department of Defense Ruth and Wheat clusters using GPU resources. Using 40 NVIDIA A100 GPUs, the simulation completes 40 characteristic diffuser-flow-convection times in 24 hours, utilizing the distance between the throat and AIP.

IV. Base Flow Characteristics

Li et al. [24] discussed the base flow of a nearly identical diffuser in detail, including the main features of the flow topology at the AIP that was associated with the evolving vortical structures in the flow that bring about losses in total pressure. These losses are characterized using the total pressure recovery and the surface-averaged circumferential distortion parameter as an indicator of the total pressure nonuniformity. As discussed by Li et al. [24], the base flow at the diffuser's AIP is characterized by a strong total pressure deficit domain along the flow path from the inner surface of the bend section. This deficit is associated with an accumulation and advection of streamwise vorticity concentrations of opposite senses along the inner surfaces of the bend about its center plane of symmetry. The formation of these streamwise vorticity concentrations is associated with tilting of vortex lines in the spanwise boundary layers on the bend's inner surfaces during the flow turning. These streamwise vorticity concentrations are transported azimuthally by characteristic counter-rotating Dean circulations that are engendered by an instability of streamwise flow through a bend. The circulation-induced concentrations of streamwise vorticity of opposite sense are advected with the streamwise flow and roll to form a time-averaged counter-rotating streamwise vortex pair associated with the domains of total pressure deficit at the AIP. Another interesting feature of the base flow is apparent along the outer bend surface, where a weak but detectable array of vortical concentrations is noted. These are consistent with the development of Görtler vortices [30] that form due to instability of the boundary layer flow over the concave surface of the outer bend.

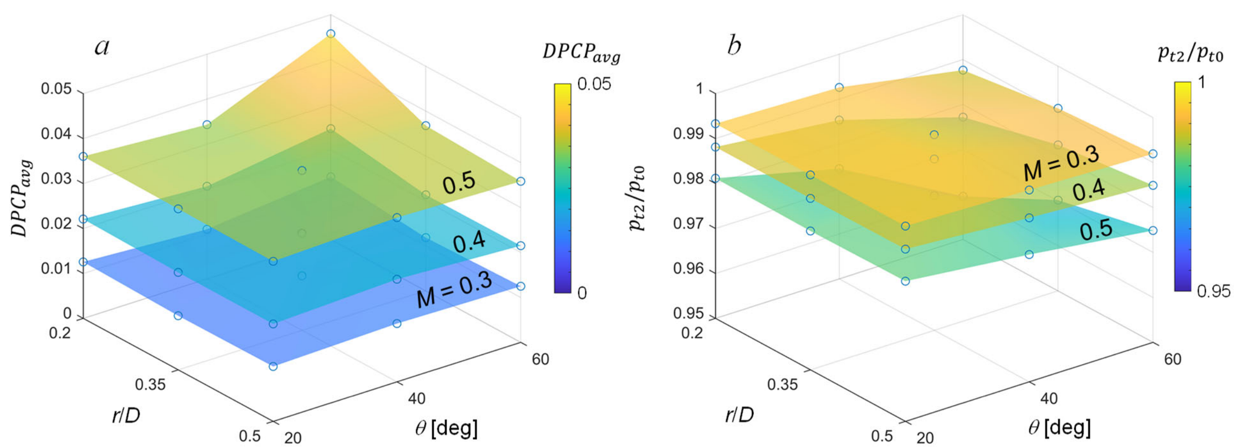

Figure 4. *Variation with bend angle θ and radius r/D of the nine variants of the bend geometry of the circumferential distortion (a) and of the total pressure recovery (b) in the base flow at M = 0.3, 0.4, and 0.5.*

The variation of the circumferential distortion parameter $DPCP_{avg}$ and the pressure recovery distributions for the nine bend geometries are summarized in Figure 4 at three characteristic Mach numbers M_{AIP} = 0.3, 0.4, and 0.5. As expected, $DPCP_{avg}$ (Figure 4a), defined as an average over the five rings of total pressure probes $DPCP_i$, i = 1–5, [25] is strongly dependent on the Mach number across all the geometries, exhibiting proportional, but not linear, dependence. In principle, the dependence of the distortion parameter on the flow geometry is similar for a given Mach number regardless of its magnitude indicating similar flow physics over this range of Mach numbers. In general, for a given Mach number, the distortion parameter remains fairy invariant with changing bend radius r/D at the two lower bend angles, maintaining the distortion levels of $DPCP_{avg}$ = 0.012, 0.022, and 0.036, with increasing Mach number. However, for the highest bend angle, θ = 60°, the distortion is inversely proportional to the radius ratio r/D. While this increase is nearly negligible for the highest r/D = 0.5, it increases by about 30% from r/D = 0.35 to r/D = 0.2. The distributions of the pressure recovery in Figure 4b indicate, as expected, a general trend of decreasing recovery with increasing Mach number, leading to the maximum loss of about 4% in total pressure at the highest Mach number at the highest bend angle and the lowest radius, which is also marked by the highest distortion in Figure 4a. Figure 4b also indicates a stronger dependence of the recovery to the bend angle than on the bend radius, although additional total pressure loss from varying θ = 20° to 60° is always less than 1% and often in the range of 0.5%. Similar to the changes in distortion, recovery dependence on the bend radius is only secondary, indicating a measurable but weak increase with increasing r/D.

V. Flow Control Effects

As discussed in §I, the findings of Li et al. [24] suggested that the application of flow actuation upstream of the bend might be too far upstream, preceding the formation and advection of streamwise vorticity in the base flow through the bend. While the actuation is potentially more effective within the bend, the present effort focuses on fluidic actuation just downstream of the bend exit for efficiency, enabling testing of each of the nine bend configurations using a single flow control module. A schematics rendition of the flow control module installed downstream of the bend is shown in Figure 5a. As shown, the actuation is applied using three independent modules, one across the inner-bend surface (A), and one (B) on each side of the rectangular cross section. Each jet array module comprises a plenum module driven by compressed air and a jet array module that is driven uniformly by the plenum. The actuation modules can be easily installed or removed from the diffuser, and the jet modules can be reconfigured by disabling individual jets. The jet array along the downstream edge of the bend inner (convex) surface consists of 14 yawed rectangular surface jets (7 on each side) having orifices that are 1.3 mm wide and 1.7 mm in height. The jets are yawed at 55° relative to the streamwise direction to induce streamwise vorticity concentrations of opposing sense to the streamwise vorticity in the base flow (cf. Figure 1). The two shorter jet arrays along the sides of the module are symmetric across the midplane and include 5 jets on each side that are also yawed (55°) to manage the formation and transport of streamwise vorticity along the side walls.

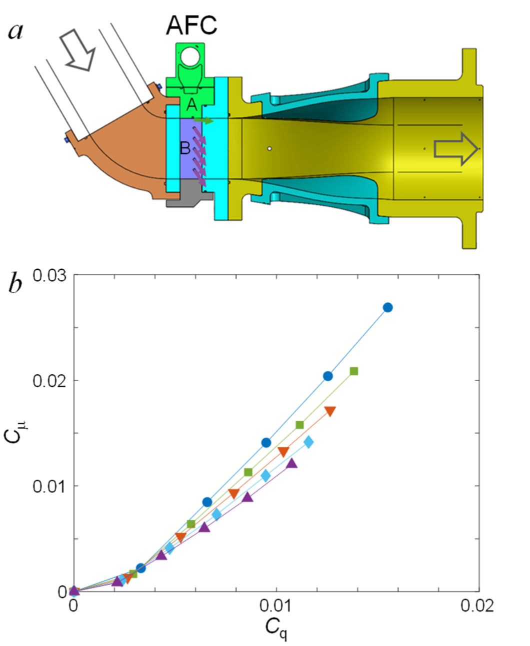

Figure 5. *a) CAD rendition of control modules A and B integrated downstream of the bend, and b) Variation of the bench-calibrated jet array momentum coefficient with the mass flow fraction of the actuation relative to the diffuser flow at M = 0.3 (●), 0.35 (■), 0.4 (▼), 0.45 (◆), and 0.5 (▲).*

The fluidic control module A was bench tested and characterized, and the three components of its thrust were measured and calibrated over a range of actuation mass flow rate $\dot{m}_j$ to obtain $|\vec{T}| = f(\dot{m}_J)$. These data were used to compute the actuation mass flow rate coefficient $C_q = \dot{m}_J/\dot{m}$ and the (thrust-based) momentum coefficient $C_\mu^F = |\vec{T}|/|\vec{P}|$, where $\dot{m}$ and $\vec{P}$ are the diffuser's mass flow rate and momentum rate, and $\dot{m}_J$ and $\vec{T}$ are the jet's mass flow rate and thrust. The variation of C_μ^F with C_q over a range of the M_{AIP} is shown in Figure 5b. As noted in [31], as expected, the force-based momentum coefficient C_μ^F varies quadratically with C_q. As shown in Figure 5b, the highest levels of C_q ($\approx$ 1.6%) and C_μ^F ($\approx$ 2.7%) are attained at the M_{AIP} = 0.3 and diminish respectively with increasing M_{AIP} to 1.1% and 1.3% at M_{AIP} = 0.5.

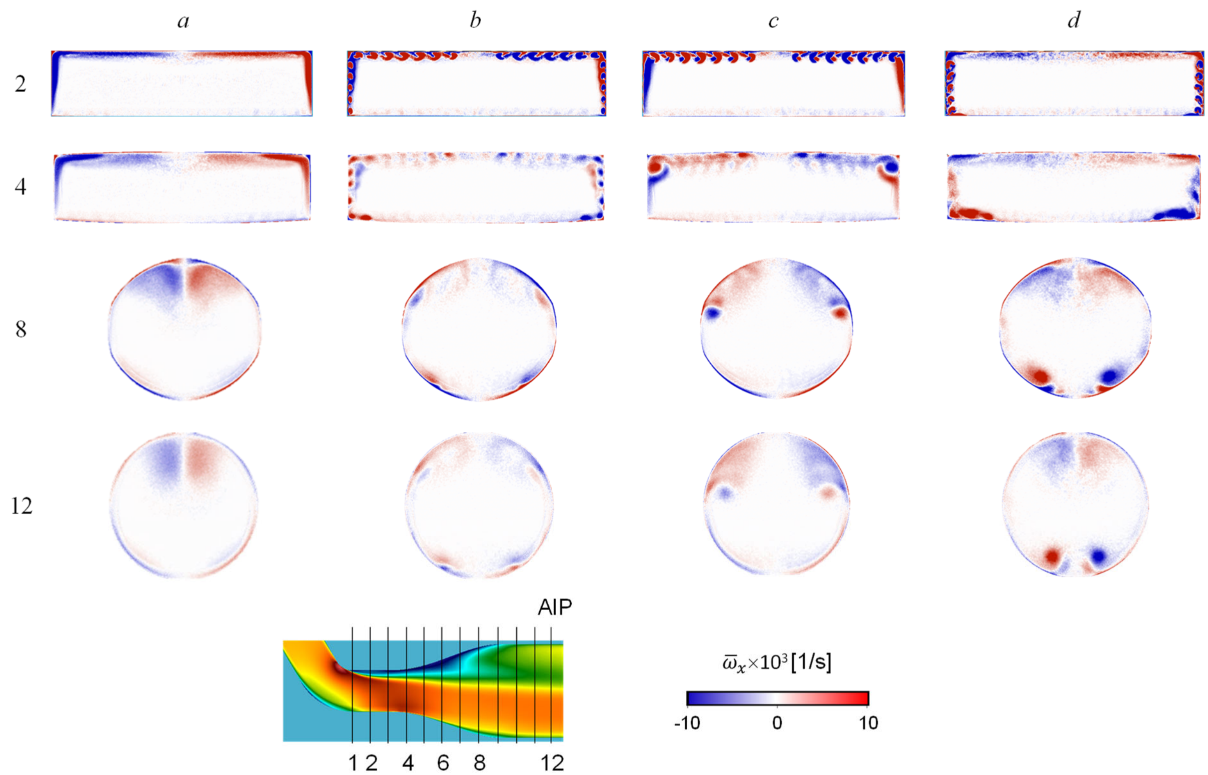

Figure 6. *Color raster plots of the time-averaged streamwise vorticity across four cross-sectional planes downstream of bend for the base flow (a), actuation modules A and B (b), module A only (c), and module B only (d) for C_q = 0.015 at M_{AIP} = 0.4, r/D = 0.2, and $\theta = 60°$.*

The streamwise evolution of the time-averaged streamwise vorticity for cross-sectional planes downstream of bend is shown in Figures 6a-d for the base flow and three AFC configurations. The base flow (Figure 6a) shows the strong vorticity components that originate along the side walls in the bend due to the Dean circulations as depicted in 6a-2. This vorticity is transported up and around the top wall (in 6a-4) and ultimately forms the characteristic counter rotating vortex pair at the AIP in 6a-12. As noted in §I, the flow control objective is two-fold. First, to suppress the advection of streamwise vorticity concentrations that form on the inner surfaces of the bend by the Dean Circulation (cf. Figure 6a-1) and second, to inject streamwise vorticity concentrations of the opposite sense to the advected vorticity for cancellation of that of the baseline flow. When the top and side jets are turned on, as shown in Figure 6b, the injection of opposite sense vorticity is clearly visible in 6b-2. Farther downstream, at 6b-4, the vorticity sense on the walls is flipped compared to the base flow resulting in smaller concentrations of time-averaged vorticity, and the transport of the surface vorticity into the core flow is significantly reduced. When the top wall jets only are active in Figure 6c, the sense of vorticity is flipped along the top wall compared to the base flow in 6c-4. This stifles the transport of vorticity up the side walls, which results in concentrations of vorticity that remain attached to the side walls. As the flow evolves towards the AIP, that vorticity that had originally formed the counter rotating vortex pair in the base flow is now reduced to small segments on the left and right halves of the AIP. In the final AFC configuration, only the side wall jets are active, shown in Figure 6d. Again, where the jets inject the opposite sense of vorticity, there is a clear flip in the vorticity sense compared to the base flow. While there is a clear reduction in vorticity magnitude along the top wall, it is not eliminated, and a weak counter-rotating vortex pair still forms as the flow evolves, as shown in 6d-8 and 12. Interestingly, the lower jets are ejecting flow into the lower vorticity region as shown in 6d-2, and this results in the transport of a strong vorticity concentration along the bottom surface of the duct. This is detrimental since it leads to the formation of a strong counter-rotating vortex pair at the bottom of the AIP highlighting the need to regulate the actuation flow rate in practical implementations for optimal performance and efficient use of the bleed air in airborne applications.

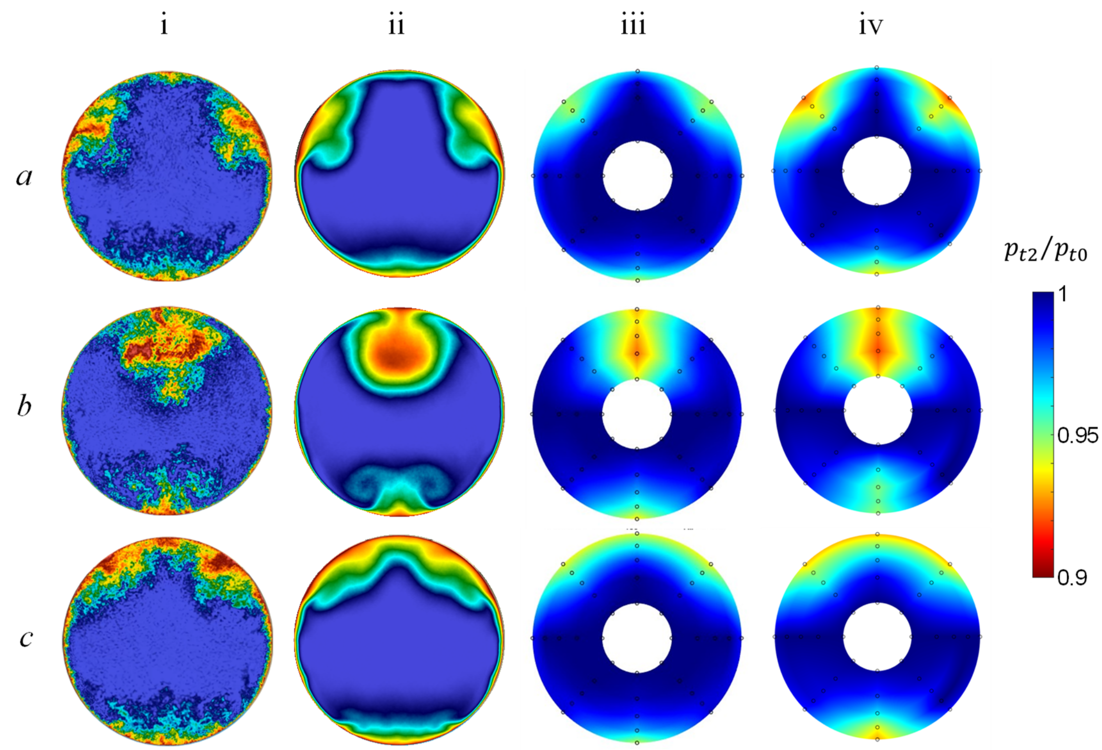

Figure 7. *Columns of color raster plots total pressure at the AIP. Numerical: instantaneous (column i), time averaged full grid (ii) and subsampled to 40 probe rake (iii), and time-averaged experimental (iv) at M_{AIP}=0.4 controlled by jet actuation module A (a), module B (b) and modules A and B at C_q=0.015 with the bend θ = 60° and r/D = 0.2.*

Simulations of instantaneous (i), time-averaged (ii), the 40-probe down-sampled (iii) distributions of the pressure recovery at the AIP are shown in Figures 7-i, ii, and iii, respectively for each of the three jet arrays discussed in connection with Figure 6 along with corresponding distributions of the time-averaged measurements using the 40-probe rake in Figures 7-iv. In row a of Figure 7, only the top jets are active, resulting in pressure deficit at the sides of the AIP, forming a two-lobed structure with a deficit near the wall, and a smaller lobe penetrating further into the core flow. This structure correlates strongly with the vorticity structure shown in Figure 6. The down-sampled raster plot mimicking the 40-probe rake does not capture many of the details but does capture the deficits at the left and right sides of the AIP. While the numerical results agree well with experimental pressure recovery trends, the magnitude is underpredicted on the walls. In row b of Figure 7, only the side jets are active, and the stronger vortex pair results in a large pressure deficit in the core flow similar to that in the base flow. Furthermore, the excess vorticity seen in Figure 6, is transported along the bottom surface, resulting in a strong pressure deficit. This feature is captured by both the measured and simulated 40-probe data. In row c of Figure 7, both the top and side jets are active, resulting in a relatively uniform pressure deficit along the top of the AIP that correlates well with the vorticity contours in Figure 6 indicating weakened vortical structures having nearly uniform vorticity distributions along the top surface of the AIP. These features are captured by the numerical and experimental rake data along the top surface.

As noted by Li et al. [24], controlling the diffuser flow upstream of a bend of $\theta = 60°$ and $r/D = 0.2$ at $M_{AIP} = 0.5$ was found to be challenging. Therefore, the effects of the actuation downstream of this configuration are illustrated in Figure 8 using distributions of the total pressure measured at the AIP when actuation is applied only along the top/inner-bend surface (actuator module A), only along the sides (side modules B), and with all of modules combined, for $M_{AIP} = 0.5$ and $C_q = 0.004$, 0.009, and 0.013 (the total pressure of the base is also shown in Figures 8a for reference). The base flow clearly exhibits a rather dramatic total pressure deficit over the central upper domain, along with a secondary localized deficit on the opposite side. This total pressure distribution results in a total pressure loss of about 4.5% and a circumferential distortion $DPCP_{avg} \approx 0.046$. At the lowest level of actuation, in row b of Figure 8, actuation using module A (Figure 8b-i) clearly displaces the total pressure deficit domain towards the surface of the AIP. In essence, it appears that the distribution in

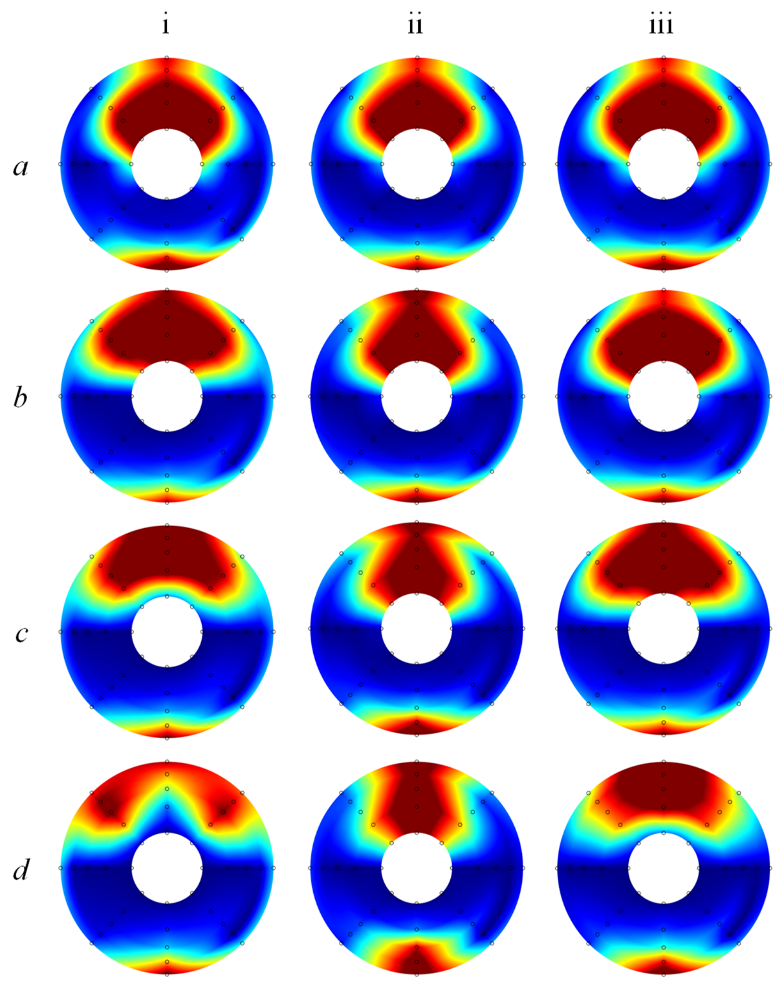

Figure 8. Color raster plots of the total pressure distributions measured at the AIP *at $M_{AIP} = 0.5$ in the presence of actuation with module A (Column i), module B (Column ii) and modules A and B (Column iii) at $C_q = 0$ (a), 0.004 (b), 0.009 (c), and 0.013 (d) for the bend $\theta = 60°$ and $r/D = 0.2$.*

the base flow is compressed radially and extended azimuthally. When actuation is applied only by the side control modules (B, Figure 8b-ii), the main effect is the narrowing of the deficit domain by suppressing its azimuthal extent. Interestingly, when all the flow control modules are active simultaneously, the resulting total pressure topology closely resembles that of the base flow (Figure 8b-iii). It should be noted, though, that since the total C_q is the same for all actuation configurations, the lowest C_q per jet is effected with all the modules activated, while the highest C_q per jet results when using only the side jets. Overall, there are only negligible changes in the distortion and recovery at $C_q = 0.004$. However, already at $C_q = 0.009$ (Figure 8c), the changes effected by isolated top and side-surface actuators are amplified as manifested by higher radial (Figure 8c-i) and azimuthal (Figure 8c-ii) compression of the deficit region, with even the simultaneous actuation by all control modules, resulting in overall compression of the total pressure deficit domain. Finally, at $C_q = 1.3\%$, actuation with module A not only compresses the deficit region but also splits it into two lobes, while significantly weakening the deficit, as seen in Figure 8d-i. This significant change in the topology of the pressure distribution is reflected in higher recovery (about 1%) and a drop in average circumferential distortion (by about 45%). It is noteworthy that, while the azimuthal deficit compression continues when only the side actuation is used (Figure 8d-i), combined actuation by modules A and B results in a combined effect where the deficit domain becomes compressed both radially and azimuthally, without being redistributed into two lobes (Figure 8d-ii).

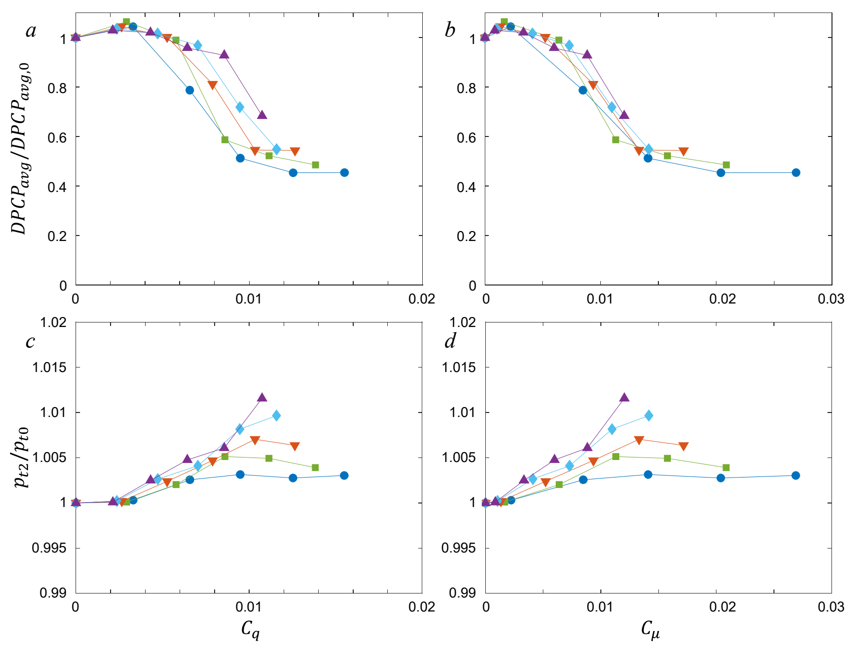

Figure 9. *Variation of the distortion parameter $DPCP_{avg}$ (a, b) and pressure recovery p_{t2}/p_{t0} (c, d) with actuation mass flow rate (a, c) and momentum (b, d) using jet actuation module A at M = 0.3 (●), 0.35 (■), 0.4 (▼), 0.45 (◆), and 0.5 (▲).*

A summary of the global effects of actuation using module A (top jet array) with the bend $\theta = 60°$ and $r/D = 0.2$ is shown in Figure 9 using the variations with actuation C_q and C_μ^F of the average circumferential distortion and pressure recovery assessed relative to the base flow for $0.3 < M_{AIP} < 0.5$. The distortion data are clustered together and follow the same general trend (Figure 9a), where there is a slight uptick in distortion for the lowest level of the mass flow rate coefficient. This indicates that the actuation is insufficient for altering the base flow and, instead, adds to the flow unsteadiness and distortion. Past $C_q = 0.003$, the control begins to affect the base flow, with flow at $M_{AIP} = 0.3$ being the most responsive. At the higher Mach numbers, there is a progressive delay in responsiveness with increasing M_{AIP} such that at $M_{AIP} = 0.5$, the flow responds with a sharp drop in distortion only past $C_q = 0.008$. Overall, several consecutive stages of the AIP distortion response to actuation are seen, beginning with a slightly detrimental uptick, followed by a delay in the drop that is proportional to M_{AIP}. At the end of the drop in actuation effectiveness, only the flow at M_{AIP} = 0.3 appears to reach an asymptotic state leveling at a decrease of about 50% of the base flow distortion. The flows at higher M_{AIP} seem to follow similar stages, albeit without reaching the asymptotic distortion levels within the present range of C_q. While the variation in relative distortion with C_q exhibits similar trends compared to the variations with C_μ^F in Figure 9b, the data in Figure 9b indicate smaller deviations between the flows at the different M_{AIP} and near-collapse of the curves. In this "collapsed" form, the initial uptick in distortion is limited to momentum coefficient of $C_\mu^F \approx 0.001$, a weak response to actuation follows to up to $C_\mu^F = 0.008$, beyond which there is a sharp drop in distortion up to the asymptotic level of $0.45 \cdot DPCP_{avg,0}$ at $C_\mu^F = 0.02$. The recovery data, however, do not show any difference between referencing the actuation to C_q or C_μ^F, as shown in Figures 9c and d. Regardless of M_{AIP}, there is a general improvement in recovery within 1%.

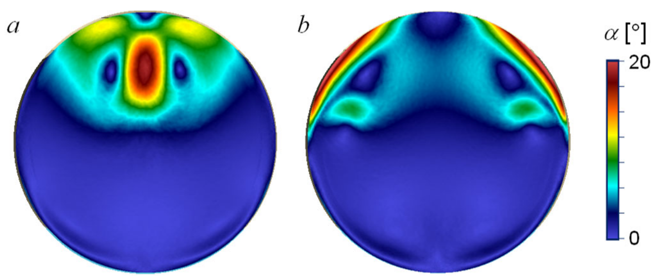

Figure 10. *Color raster plots of flow angularity at the AIP in the base flow (a) and with jet actuation module A at C_q = 0.015 (b), M = 0.4.*

Finally, distributions of the flow angularity, measured by the angle of the time-averaged flow velocity vector relative to the streamwise direction at the AIP, are shown Figure 10a and b in the absence and presence of actuation, respectively. Figure 10a shows angularity that peaks at about 20° on the center plane of the duct that coincides with the strongest in-plane induced downward velocity by the counter-rotating vortex pair towards the AIP centerline (cf. Figure 6). When the actuation is applied by the top jet array (A) by C_q = 0.015 (Figure 10b), the angularity is primarily induced by the vortical structures shown in Figure 6 and has lower peaks within the flow (up to about 6°) and higher peaks in a narrow domain along the side walls.

VI. Time-resolved Flow Analysis

The present, time-resolved, numerical simulations provide the temporal evolution of the flow within the diffuser. The evolutions of the time-averaged and instantaneous streamwise vorticity concentrations in the absence and presence of actuation (using actuation module A) are compared in Figure 11 (α = 60°, r/D = 0.2, M_{AIP} = 0.4, and C_q = 0.015). Similar to the data in Figure 6, the time averaged vorticity concentrations in the base flow and in the presence of actuation (Figures 11a and b, respectively) depict clear, organized images of clockwise (CW) and counter-clockwise (CCW) vortical structures in the diffuser sections between the bend and the AIP (Sections 1 – 12, cf. Figure 6). However, the distributions of the corresponding streamwise vorticity in the instantaneous flow (Figure11c and d) are markedly different and are characterized by small-scale intermingled strands of CW and CCW vorticity that form the time-averaged distributions in Figures 11a and b. The time-averaged and instantaneous vorticity concentrations in the base flow are reasonably similar along the side walls in Sections 1 and 2 (Figures 11a-1, -2 and 11c-1, -2). In Section 2 some reorganization of the instantaneous vorticity strands is visible on either side of the top/inner surface, where the CW and CCW vorticity concentrations are dominant along the left and the right sides, respectively and begin to accumulate about the center plane. However, the advection of these vorticity strands towards the center of the diffuser cross sections farther downstream is marked by mixed concentrations of CW and CCW sense that apparently give rise to coherent vortical structures only in the time-averaged flow. Similar patterns also exist in the presence of actuation (11b and d). While there is similarity between the time-averaged and instantaneous distributions in Section 2 (Figures 11b-2 and d-2), showing the injection of strong concentrations of CW and CCW vorticity, the time-averaged and instantaneous distributions bear little resemblance farther downstream. Specifically, as discussed in connection with Figure 6, when the time-averaged flow enters the short diffuser, in §4 (Figure 11b-4), there are strong corner vorticity concentrations that limit the transport of the side wall vorticity and its accumulation on the top surface in contrast to the base flow in Figure 11a-6. However, the instantaneous concentrations are far less structured and are characterized by a mixture of CW and CCW vorticity strands on both sides of the duct. Two effects of the actuation are clearly apparent in the instantaneous images as well. First, there is a diminution of the accumulation of vorticity near the top surface that gives rise to the strong counter-rotating vortex pair in the time-averaged flow that is replaced by accumulation on the sides of the duct, and second, an overall reduction in the intensity of the remaining concentrations in the presence of actuation, as is evident in Figure 11c-8, -12 and 12d-8, -12.

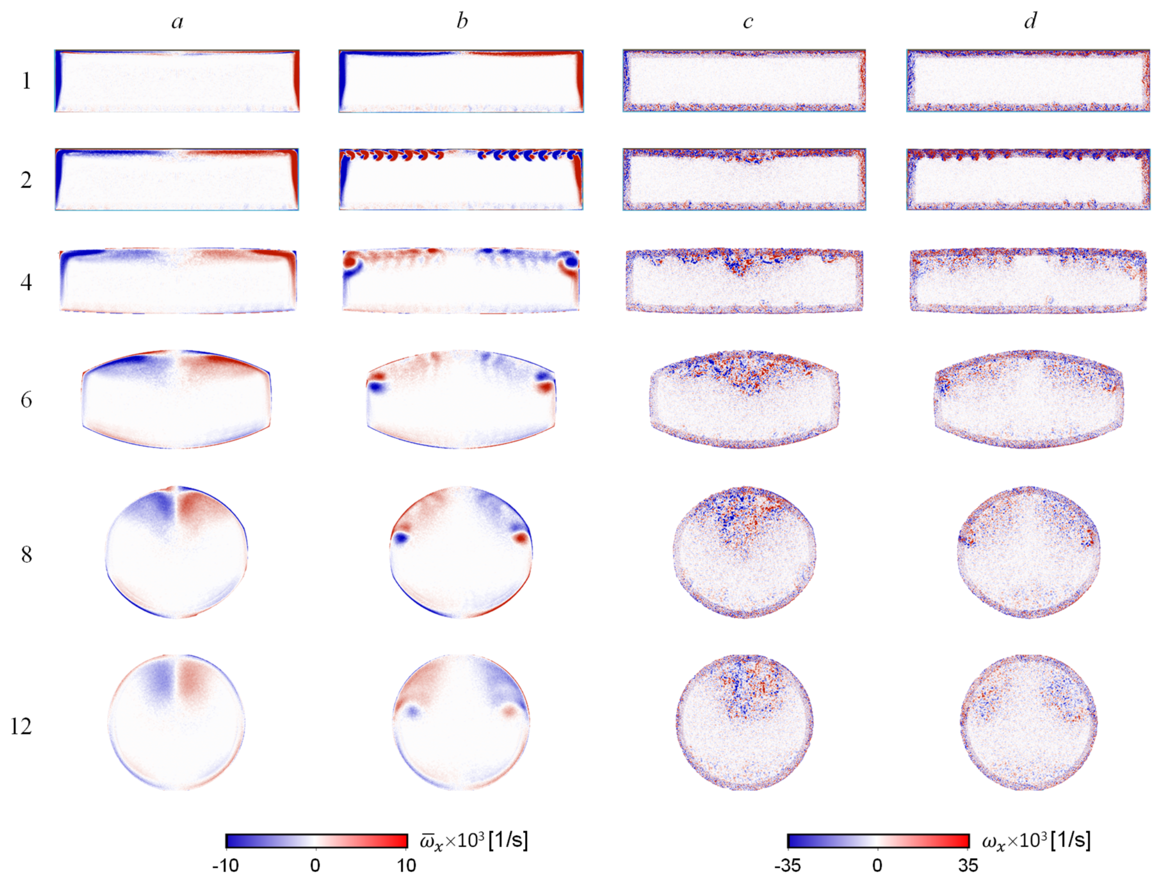

Figure 11. *Time-averaged and instantaneous streamwise vorticity in the cross-sectional planes of Figure 6 for the base flow (a, c) and with jet actuation module A at $C_q = 0.015$ (b, d).*

Following the discussion of Figure 11, the instantaneous data enables assessment of the temporal variations in the circulation of the opposite sense vorticity strands in cross sections of the flow. At a given cross section, the circulation is assessed in each of the two section halves about the central plane of symmetry that are each dominated by single-sense vorticity in the time-averaged flow. The time trace of the total sectional circulation is also included. Figures 12a and c show the three time-traces of the circulation (cf. Figure 6) for the base flow and in the presence of actuation, respectively, and their corresponding power spectra are shown in Figures 12b and d, respectively. As expected, the time traces of the circulation in each half plane (left and right are marked blue (CW sense) and red (CCW sense), respectively) of the base flow (Figure 12a) show that the mixture of CW and CCW vorticity strands gives rise to single-sense circulation in accord with the sense of vorticity in the time-averaged flow (and having the same time-averaged circulation) and the time-averaged total sectional circulation is indeed zero. Due to the short time sequence of the simulations, the power spectra of the circulation have a rather coarse frequency resolution. The three spectra of the circulation time-traces in the base flow (Figure 12a) exhibit similar energy distributions that diminish by about an order of magnitude at the highest resolved frequency. The corresponding time traces of the circulation in the presence of actuation in Figure 12c exhibit a remarkable characteristic. As noted in §III, the actuation in the present investigations is designed to counter the formation of the streamwise vorticity concentrations by the Dean circulations on either half of the cross section. The traces in Figure 12b show that in the presence of actuation the circulations in each half plane reverses its sign, indicating that the actuation locally overwhelms the wall vorticity induced in the base flow, and, moreover, the magnitude levels are about double those in the base flow. This reversal also indicates that the actuation level control may be too high ($C_q = 0.015$ in the simulations). It is also noteworthy that in the presence of actuation, the time traces of the circulation show evidence of smaller-scale structures as is expected immediately downstream of the actuation jets. This is evidenced in the spectral content in Figure 12d that also shows that the spectral peaks of the total circulation are higher than the circulation of each half-plane.

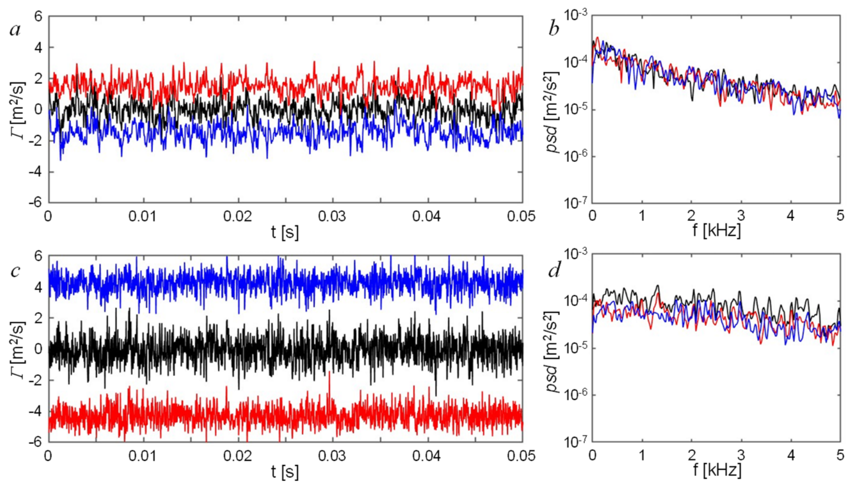

Figure 12. *Time traces of the circulation at the on the short diffuser inlet plane: left half (red), right half (blue) and total (black) for the base flow (a), and with jet actuation module A at $C_q = 0.015$ (c). Power spectra of the circulation traces in the base flow (b) and in the presence of actuation with module A (d).*

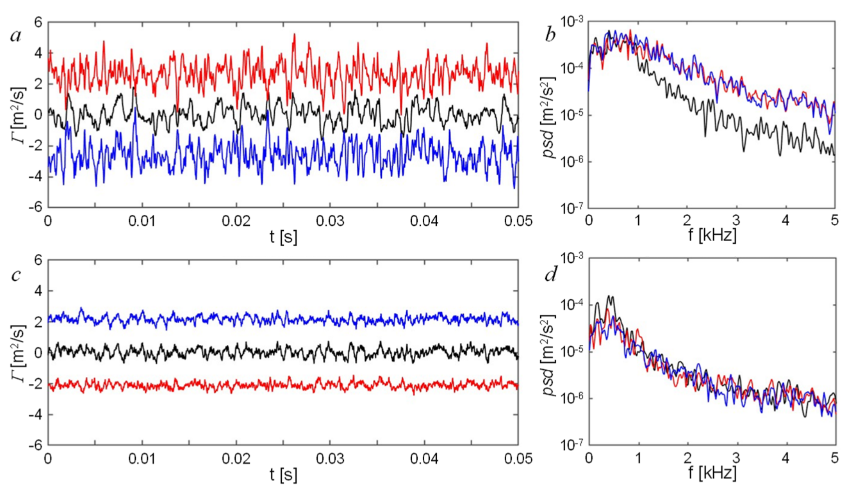

Figure 13. *As in Figure 12, at the AIP.*

Similar analysis at the AIP (Section 12, Figure 13) shows similar trends with some significant differences.

The time traces of the circulation in the base flow (Figure 13a) show that the time-averaged level of the trace in each half-plane increases at the AIP by about 50%, indicating that the streamwise vorticity concentrations intensify by transport of streamwise vorticity from the inner surfaces of the duct. In addition, there is a notable increase in the amplitude of the fluctuations at the AIP on both half-planes. The power spectra of the circulation traces (Figure 13b) show the increased spectral peaks at lower frequencies (around 800 Hz) with somewhat faster decay of the higher spectral components, especially in the total circulation, suggesting that the fluctuations across the central plane are out-of-phase. In the presence of actuation, the sense of the circulation in Figure 13c is reversed as in Figure 12 and there is a significant decrease in its time-averaged levels compared to the effects in Figure 12c. Another important feature is the remarkable suppression of the small-scale (high frequency) fluctuations in the time traces that may be indicative of the dissipative effects of the actuation. The persistent switch in the sense of the circulation at the AIP (albeit at lower levels than farther upstream) is another indication that the level of the actuation ($C_q = 0.015$) is probably too high and can be adjusted to yield zero or near-zero net circulations in both half-planes (and overall). Comparison between the spectral energy in the presence of actuation in Figures 13d and 14d shows lower-level spectral peaks overall, by over an order of magnitude and higher decay rate with increasing frequency in the presence of actuation.

VII. Variations of the Jet Actuation Array

As noted in §§V and VI, the investigations of the effects of actuation using the full, 14-jet array of module A indicated that the formation of opposite sense concentrations of streamwise vorticity downstream of the bend could overwhelm the natural advection of streamwise vorticity by the Dean circulations in the base flow (e.g., Figure 11 Column b). Preliminary investigations were conducted to explore the effects of fewer actuation jets in the module A array and changes in the mass flow rate per jet by using a smaller array of the 8 central jets with three inactive end jets at each spanwise end of the array. The effects of the reduced array are compared with the effects of the full 14-jet array at $M_{AIP} = 0.5$ in Figure 14. Two sets of comparisons of the 14-jet array (14a, b, and e, f) and 8-jet arrays (14c, d, and g, h) are shown. In Figures 14a-d, the 14-jet (14a, b) and 8-jet (14c, d) arrays are

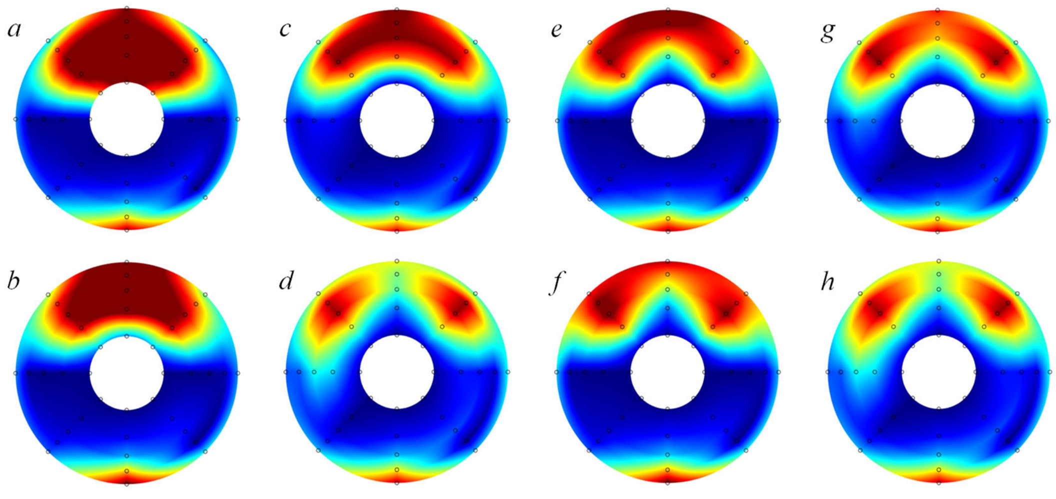

Figure 14. Color raster plots of the *total pressure at the AIP with module A actuation for bend $\theta = 60°$ and r/D = 0.2 at M_{AIP}= 0.5 using 14-jet (a, b and e, f) and 8-jet (c, d, and g, h) actuation arrays. In a, c the arrays are operated at $C_q = 0.0043$ and in b, d the arrays are operated at $C_q = 0.0086$. (a, c), and 0.009 (b, d). In e-h, the 14-jet and 8-jet arrays are compared at nearly the same C_q/jet: in e, g C_q/jet = 0.00077 and 0.008, respectively and in f, h C_q/jet = 0.00091 and 0.0011, respectively.*

compared at nearly the same actuation C_q, where $C_q = 0.0043$ and 0.0086 in Figures 14a, c and 14b, d, respectively. The total pressure distributions clearly show changes in the distributions and reductions in deficit with the 8-jet array, although they are operated at larger C_q/jet. Indeed, the corresponding $DPCP_{avg}$ diminishes from 0.043 to 0.026 in Figures 14a, c, and from 0.032 to 0.021 in Figures 14b, d. In Figures 14e-h, the 14-jet (14e, f) and 8-jet (14g, h) arrays are compared at nearly the same C_q/jet where C_q/jet = 0.00077 and 0.008 in Figures 14e, g, respectively and in C_q/jet = 0.00091 and 0.0011 in Figures 14f, h, respectively. These data show that at lower overall C_q, the 8-jet array leads to higher diminution in total pressure losses at nearly the same C_q/jet, indicating that adjustments in the distributions of the jets within the array and in the actuation mass flow rate per jet (perhaps even in real time) can improve the performance of this flow control approach.

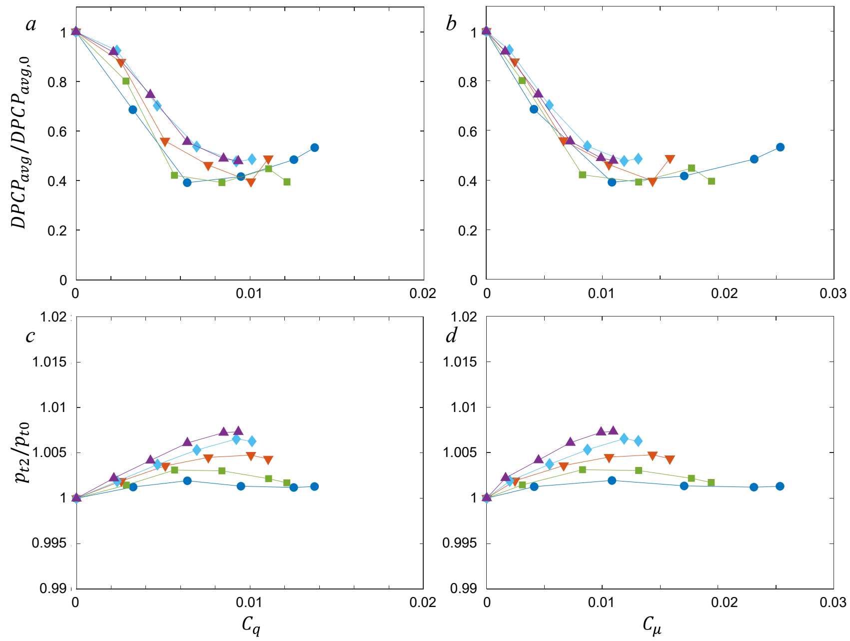

Figure 15. *As in Figure 9, with the central 8-jet array of actuation module A.*

Similar to the performance of the 14-jet array (Figure 9), detailed analysis of performance of the 8-jet array in terms of $DPCP_{avg}$ and recovery relative to the base flow at $M_{AIP} = 0.3$, 0.35, 0.4, 0.45, and 0.5 is shown in Figure 15. The main difference compared to the 14-jet array is in the response of the flow to the onset of actuation. Instead of a small increase in distortion with the onset of the actuation followed by weak response until higher actuation levels are attained with the 14-jet array (Figure 9), the response to the 8-jet array is immediate upon activation of the actuation and therefore similar levels of distortion suppression can be achieved at lower actuation mass flow rate. For instance, a reduction of 40% in $DPCP_{avg}$ that is effected by $C_\mu^F = 0.0122$ with a 14-jet array (Figure 9b) can be attained with $C_\mu^F = 0.0062$ with the 8-jet array (Figure 15b). Furthermore, compared to the 14-jet array, the 8-jet array reaches the asymptotic level of $DPCP_{avg}$ at a lower $C_\mu^F = 0.014$ (*vs*. 0.02) and at 40% the distortion of the base flow (*vs*. 45%). The corresponding variations of the recovery with C_q and C_μ^F (Figures 15c and d) are somewhat lower than with the 14-jet array (Figures 9c and d) but still demonstrate a gain.

VIII. Conclusions

A fluidic flow control approach for mitigation of total pressure distortion at the AIP of an aggressive compact diffuser was developed in a joint experimental/numerical study. This control approach targets the evolution of streamwise vorticity concentrations that originate in the bend section of the diffuser and result in total pressure losses and distortion at the AIP, and builds on the earlier findings of Li et al. [24] who associated these losses with the formation of a pair of counter-rotating streamwise vortices formed by the advection of wall streamwise vorticity from the inner surfaces of the diffuser bend and its downstream sections by Dean circulations within the bend flow.

The present control approach seeks to suppress spanwise advection of streamwise vorticity concentrations of opposite sense along the inner surfaces of the diffuser on both sides of its plane of symmetry that can accumulate and roll up to counter-rotating concentrations, by injecting streamwise vorticity concentrations of the opposite sense to the advected surface vorticity for its cancellation. These effects are realized by a spanwise array of surface yawed jets on each side of the plane of symmetry to block the advection induced by the Dean circulations, while each yawed jet in the array forms a surface-bound streamwise vortex having an opposite send to the advected streamwise vorticity. In the present investigations, independently controlled jet arrays were integrated in the diffuser section downstream of the bend along its inner radius surface and along its side walls. Opposite pairs of these arrays were operated in three primary configurations, namely along the inner surface of the diffuser (A), along its side walls (B), and in concert. It was shown that each of these configurations successfully mitigated the total pressure distortion to some degree. Furthermore, the numerical simulations confirmed that the small-scale concentrations of streamwise vorticity injected by the actuation jets could reduce the transport of vorticity concentrations induced by the bend circulations. The experiments showed that configuration A was the most efficient and yielded a reduction in the distortion descriptor $DPCP_{avg}$ by 45% at $M = 0.5$, for the most aggressive flow path at a bend angle and radius $\theta = 60°$ and $r/D = 0.2$, by utilizing a total actuation mass flow rate of just over 1.2%.

Temporal numerical analysis of the instantaneous flow showed that the distributions of the instantaneous streamwise vorticity in cross sections of the flow were markedly different from the corresponding time-averaged vortical structures. The instantaneous distributions are characterized by small-scale intermingled strands of CW and CCW vorticity whose advection towards the center of the diffuser's cross sections appears to be rather disordered, but they yield the coherent large-scale structure when averaged over large number of realizations, but the time-averaged and instantaneous distributions bear little resemblance farther downstream. Similar patterns also exist in the presence of actuation. However, the actuation leads to diminution of accumulation of vorticity about the plane of symmetry that gives rise to the strong counter-rotating vortex pair in the time-averaged flow that is replaced by accumulation on the sides of the duct. Furthermore, the actuation leads to an overall reduction in the intensity of the remaining instantaneous vortical strands implying stronger diffusion. Comparison of time traces of the circulation in each half of the AIP section about the plane of symmetry showed that the time-averaged level of the circulation trace in each half-plane of the AIP increases along the diffuser, indicating the intensification of the transport of streamwise vorticity from the inner surfaces of the duct with a notable increase in the amplitude of the fluctuations at the AIP. In the presence of actuation, the sense of circulation in the base flow is reversed and there is a significant decrease in the time-averaged levels. Another important feature is the remarkable suppression of the high-frequency fluctuations in the time traces associated with the effects of the actuation.

Finally, the effects of changes in the number and position of the actuation jets were investigated in limited experiments where the original spanwise actuation of configuration A (14 jets) was replaced with an 8-jet array. It was shown that this configuration improved the reduction of distortion by reducing $DPCP_{avg}$ at $M_{AIP} = 0.5$ by about 55% and at a lower actuation mass flow rate of only 0.8%. These findings indicate that adjustments in the distributions of the jets within the array and in the actuation mass flow rate per jet can improve the performance of this flow control approach. These adjustments can be implemented in real-time control.

Acknowledgment/Disclaimer

This work was sponsored by the Office of Naval Research (ONR), under grant number N000142312500. The views and conclusions contained herein are those of the authors only and should not be interpreted as representing those of ONR, the U.S. Navy, or the U.S. Government. The authors acknowledge the computational resources provided by the Department of Defense (DoD) High Performance Computing Modernization Program, specifically the DoD ERDC and Navy DoD Supercomputing Resource Center systems.

References

[1] Connolly, B.J., Loth, E., Smith, C.F., "Unsteady Flow Simulations for Diffusing S-ducts of Circular and Rectangular Cross-section," AIAA Paper 2018-2130, 2018.

[2] Dean, W.R. "Note on the Motion of Fluid in a Curved Pipe," Philosophical Magazine*,* Vol. 4, 1927, pp. 208-223.

[3] Dean, W.R. "The Streamline Motion of Fluid in a Curved Pipe," Philosophical Magazine*,* Vol. 4, 1928, pp. 673-695.

[4] Dutta, P., Rajendran, N. K., Cep, R., Kumar, R., Kumar, H., & Nirsanametla, Y. (2025). "Numerical investigation of Dean vortex evolution in turbulent flow through 90° pipe bends," Frontiers in Mechanical Engineering, Vol. 11: 1405148, 2025.

[5] Winters, K.H., "A Bifurcation Study of Laminar Flow in a Curved Tube of Rectangular Cross-Section," Journal of Fluid Mechanics, Vol. 180, 1987, pp. 343-369.

[6] Sudo, K., Sumida, M., and Hibara, H., "Experimental Investigation on Turbulent Flow in a Square-Sectioned 90-degree bend," Experiments in Fluids, Vol. 30, 2001, pp. 246-252.

[7] Hall, G., Hurwitz, W., Tiebens, G., Norby, W., Singshinsuk, P., and Wilt, C., "Development of the F/A-18 E/F Air Induction System," AIAA Paper 93-2152, 1993.

[8] Anderson, B. H., and Gibb, J., "Study on Vortex Generator Flow Control for the Management of Inlet Distortion," Journal of Propulsion and Power, Vol. 9, 1993, pp. 422–430.

[9] Owens, L. R., Allan, B. G., and Gorton, S. A., "Boundary-Layer-Ingesting Inlet Flow Control," Journal of Aircraft, Vol. 45, 2008, pp. 1431–1440.

[10] Tanguy, G., MacManus, D. G., Zachos, P., Gil-Prieto, D., and Garnier, E., "Passive Flow Control Study in an S-Duct Using Stereo Particle Image Velocimetry," AIAA Journal, Vol. 55, No. 6, 2017, pp. 1862–1877.

[11] Scribben, A., Ng, W., and Burdisso, R., "Effectiveness of a Serpentine Inlet Duct Flow Control Technique at Design and Off-Design Simulated Flight Conditions," Journal of Turbomachinery, Vol. 128, No. 2, 2006, pp. 332–339.

[12] Anderson, B. H., Miller, D. N., Addington, G. A., and Agrell, J., "Optimal Micro-Jet Flow Control for Compact Air Vehicle Inlets," NASA/TM—2004-212937, 2004.

[13] Gartner, J., and Amitay, M., "Flow Control in a Diffuser at Transonic Conditions," AIAA Paper 2015-2484, 2015.

[14] Rabe, A., "Effectiveness of a Serpentine Inlet Duct Flow Control Scheme at Design and Off-design Simulated Flight Conditions," Ph.D. Thesis, Virginia Tech, 2003.

[15] Harrison, N., Anderson, J., Fleming, J., and Ng, W., "Active Flow Control of a Boundary Layer-Ingesting Serpentine Inlet Diffuser," Journal of Aircraft, Vol. 50, No. 1, 2013, pp. 262–271.

[16] Garnier, E., "Flow Control by Pulsed Jet in a Curved S-Duct: A Spectral Analysis," AIAA Journal, Vol. 53, No. 10, 2015, pp. 2813–2827.

[17] Amitay, M., Pitt, D., and Glezer, A., "Separation Control in Duct Flows," Journal of Aircraft, Vol. 39, No. 4, 2002, pp. 616–620.

[18] Mathis, R., Duke, D., Kitsios, V., and Soria, J., "Use of Zero-net-mass-flow for Separation Control in Diffusing S-duct," Experimental Thermal and Fluid Science, Vol. 33, No. 1, 2008, pp. 169–172.

[19] Gissen, A. N., Vukasinovic, B., McMillan, M. L., and Glezer, A., "Distortion Management in a Boundary Layer Ingestion Inlet Diffuser Using Hybrid Flow Control," Journal of Propulsion and Power, Vol. 30, No. 3, 2014, pp. 834–844.

[20] Burrows, T. J., Vukasinovic, B., Lakebrink, M. T., Mani, M., and Glezer, A., "Control of Flow Distortion in Offset Diffusers using Trapped Vorticity," International Journal of Heat and Fluid Flow, Vol. 75, 2019, pp. 122–134.

[21] Burrows, T. J., Vukasinovic, B., Glezer, A., Lakebrink, M. T., and Mani, M., "Experimental and Numerical Investigation of Active Flow Control of a Serpentine Diffuser," AIAA Journal, Vol. 59, 2021, pp. 607–620.

[22] Burrows, T. J., Vukasinovic, B., Glezer, A., Lakebrink, M. T., and Mani, M., "Controlled Flow in a Serpentine Diffuser with a Cowl Inlet," Journal of Aircraft, Vol. 62, 2025, pp. 438 – 447.

[23] Stratton, Z., Spyropoulos, J.T., Mani, M., Mace, J., Li, S., Fletcher, J., Vukasinovic, B., and Glezer, A., "Development of an Aggressive Offset Diffuser Testbed with Adaptive Design Characteristics", AIAA Paper 2025-2108, 2025.

[24] Li, S., Fletcher, J., Vukasinovic, B., Mace, J., Glezer,A., Mani, M., Stratton, Z., and Spyropoulos, J.T., "Control of Flow Circulations in a Programmable Offset Diffuser", AIAA Paper 2025-3392, 2025.

[25] Society of Automotive Engineers Inc., "Gas Turbine Engine Inlet Flow Distortion Guidelines,", 2017. ARP 1420 Rev. C.

[26] Ham, F., Mattsson, K., and Iaccarino, G., "Accurate and Stable Finite Volume Operators for Unstructured Flow Solvers," CTR Annual Research Briefs, 2006, pp. 243–261.

[27] Bres, G. A., Bose, S. T., Emory, M., Ham, F. E., Schmidt, O. T., Rigas, G., and Colonius, T., "Large-Eddy Simulations of Co-annular Turbulent Jet Using a Voronoi-Based Mesh Generation Framework," AIAA Paper 2018-3302, 2017.

[28] Kawai, S., and Larsson, J., "Wall-Modeling in Large-Eddy Simulation: Length Scales, Grid Resolution, and Accuracy," CTR Annual Research Briefs, 2010, pp. 39–46.

[29] Germano, M., Piomelli, U., Moin, P., and Cabot, W. H., “A Dynamic Subgrid-Scale Eddy Viscosity Model,” Physics of Fluids A - Fluid Dynamics, Vol. 3, 1991, pp. 1760–1765.

[30] Saric, W. S., “Görtler Vortices,” Annual Review of Fluid Mechanics, Vol.26, 1994, pp. 379–409.

[31] Vukasinovic, B., Funk, R. B., and Glezer, A., “Circulation Control Using Arrays of Fluidically Oscillating Jets,” AIAA Journal, Vol. 63, 2025, pp. 4023-4034.

[32] Burrows, T.J., Gong, Z., Vukasinovic, B., and Glezer, A. “Investigation of Trapped Vorticity Concentrations Effected by Hybrid Actuation in an Offset Diffuser”, AIAA Paper 2016-0055, 2016.